The Astrophysical Journal, 662:39–52, 2007 June 10

EXPLORATIONS OF THE *r*-PROCESSES: COMPARISONS BETWEEN CALCULATIONS AND OBSERVATIONS OF LOW-METALLICITY STARS

Karl-Ludwig Kratz,[1,2] Khalil Farouqi,[2] Bernd Pfeiffer,[2] James W. Truran,[3] Christopher Sneden,[4] and John J. Cowan[5]

Received 2006 August 24; accepted 2007 March 1

ABSTRACT

Abundances of heavier elements (barium and beyond) in many neutron-capture-element–rich halo stars accurately replicate the solar system *r*-process pattern. However, abundances of lighter neutron-capture elements in these stars are not consistent with the solar system pattern. These comparisons suggest contributions from two distinct types of *r*-process synthesis events, a so-called main *r*-process for the elements above the second *r*-process peak and a weak *r*-process for the lighter neutron-capture elements. We have performed *r*-process theoretical predictions to further explore the implications of the solar and stellar observations. We find that the isotopic composition of barium and the elemental Ba/Eu abundance ratios in *r*-process–rich low-metallicity stars can only be matched by computations in which the neutron densities are in the range $23 \lesssim \log n_n \lesssim 28$, values typical of the main *r*-process. For *r*-process conditions that successfully generate the heavy element pattern extending down to $A = 135$, the relative abundance of ^{129}I produced in this mass region appears to be at least ~90% of the observed solar value. Finally, in the neutron number density ranges required for production of the observed solar/stellar third *r*-process–peak ($A \approx 200$), the predicted abundances of interpeak element hafnium ($Z = 72$, $A \approx 177$–180) follow closely those of third-peak elements and lead. Hf, observable from the ground and close in mass number to the third *r*-process–peak elements, might also be used as part of a new nuclear chronometer pair, Th/Hf, for stellar age determinations.

Subject heading: nuclear reactions, nucleosynthesis, abundances

1. INTRODUCTION

The nature of rapid neutron-capture nucleosynthesis (the *r*-process) and its contributions to the abundances of post iron-peak elements ($Z > 30$) were first delineated in pioneering studies by Cameron (1957) and Burbidge et al. (1957). The details, however, still remain to be worked out (e.g., see Truran et al. [2002], Sneden & Cowan [2003], Cowan & Thielemann [2004], and Cowan & Sneden [2006] for recent reviews and discussion). The physics of the *r*-process involves nuclear masses, β-decay and neutron-capture (*n*-capture) rates, and fission properties of unstable nuclear species far from the region of β-stability. Laboratory conditions needed to measure properties of such exotic nuclei are very difficult to produce, but much progress has occurred over the past decade. About 50 β-decay half-lives and 10 nuclear masses have now been measured for the lighter ($A \leq 140$) isotopes in the *r*-process production path at neutron freeze-out (e.g., Kratz et al. 2000, 2005a, 2005b; Pfeiffer et al. 2001, 2002; Möller et al. 2003; Kratz 2006). Experimental data for heavier *r*-process isotopes are not yet available.

Additionally, we do not clearly understand the characteristics of the stellar or supernova environments in which *r*-process synthesis occurs. Circumstantial evidence for the synthesis of the heavy ($A \geq 130$) *r*-process nuclei in some site associated with massive stars, with lifetimes (production timescales) $\tau_{r\text{-pro}} \leq 10^8$ yr, seems compelling. Proposed sites include both an *r*-process in a high-entropy (neutrino-driven) wind from a Type II supernova (SN II; Woosley et al. 1994; Takahashi et al. 1994) and one occurring in the decompressed ejecta of neutron star mergers (Lattimer et al. 1977; Rosswog et al. 1999; Freiburghaus et al. 1999b). Better understood is the astrophysical site for the slow *n*-captures that synthesize the heaviest *s*-process nuclei (the so-called "main" component), He-fusion zones of low- and intermediate-mass asymptotic giant branch stars (see, e.g., Busso et al. 1999) of significantly longer lifetimes, $\tau_{s\text{-pro}} \geq 10^9$ yr. This difference in the timescales for heavy element enrichment makes the lowest metallicity (oldest?) halo stars attractive laboratories for empirical insights into *r*-process synthesis (Truran et al. 2002; Sneden & Cowan 2003; Cowan & Sneden 2006).

Significant numbers of very metal-poor *r*-process–rich halo giants have been discovered in the past several decades and analyzed with ever-increasing detail and accuracy. We define these stars to be Galactic halo members that have $[\mathrm{Fe/H}] \lesssim -2$,[6] *n*-capture relative overabundance factors of 10 or more (e.g., $[\mathrm{Eu/Fe}] \gtrsim +1$), and clear evidence for *r*-process dominance over the *s*-process (usually indicated by $[\mathrm{Ba/Eu}] \lesssim -0.7$). Comprehensive abundance analyses involving 10–40 *n*-capture elements have been published for individual *r*-process–rich stars by Westin et al. (2000; HD 115444), Cowan et al. (2002; BD +17 3248), Hill et al. (2002; BPS CS 31082−001), Sneden et al. (2003; BPS CS 22892−052), Christlieb et al. (2004; BPS CS 29497−004), and Ivans et al. (2006; HD 221170).

There also have been recent larger sample studies of low-metallicity *n*-capture–rich giants. Johnson & Bolte (2001) analyzed a set of 22 stars but with generally fewer *n*-capture elements per

[1] Max-Planck-Institut für Chemie, Otto-Hahn-Institut, Joh.-J. Becherweg 27, D-55128 Mainz, Germany.

[2] HGF Virtuelles Institut für Struktur der Kerne und Nukleare Astrophysik (VISTARS), D-55128 Mainz, Germany; klkratz@uni-mainz.de, farouqi@uni-mainz.de, bernd.pfeiffer@uni-mainz.de.

[3] Department of Astronomy and Astrophysics and Enrico Fermi Institute, University of Chicago, Chicago, IL 60637; and Argonne National Laboratory, Argonne, IL 60439; truran@nova.uchicago.edu.

[4] Department of Astronomy and McDonald Observatory, University of Texas, Austin, TX 78712; chris@verdi.as.utexas.edu.

[5] Homer L. Dodge Department of Physics and Astronomy, University of Oklahoma, Norman, OK 73019; cowan@nhn.ou.edu.

[6] We adopt the usual spectroscopic notations that $[\mathrm{A/B}] \equiv \log(N_\mathrm{A}/N_\mathrm{B})_\mathrm{star} - \log(N_\mathrm{A}/N_\mathrm{B})_\odot$, and that $\log \epsilon(\mathrm{A}) \equiv \log(N_\mathrm{A}/N_\mathrm{H}) + 12.0$, for elements A and B. In addition, metallicity is assumed here to be equivalent to the stellar [Fe/H] value.

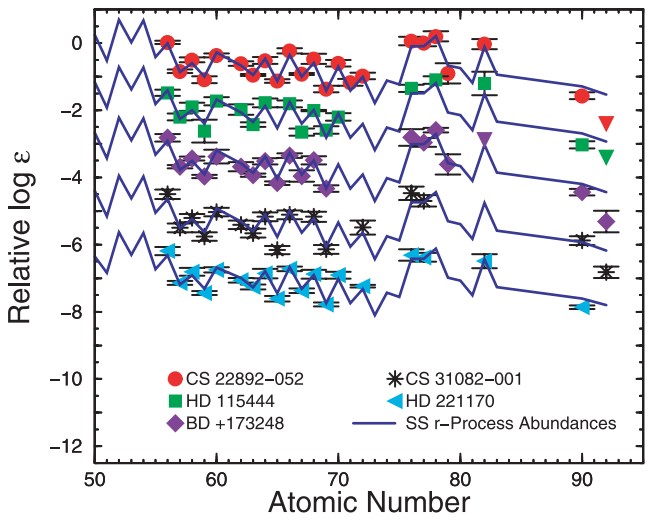

FIG. 1.—Abundances for elements with $Z \geq 56$ for five *r*-process–rich Galactic halo stars (Cowan & Sneden 2006). *Top to bottom*: CS 22892−052 (*filled circles*; Sneden et al. 2003), HD 115444 (*filled squares*; Westin et al. 2000), BD +17 3248 (*filled diamonds*; Cowan et al. 2002), CS 31082−001 (*stars*; Hill et al. 2002), and HD 221170 (*filled triangles*; Ivans et al. 2006). The vertical scale for the CS 22892−052 abundance set is true, and abundances of all of the stars have been vertically scaled downward for display purposes. Each of these stellar abundance sets is overlaid with the scaled SS *r*-process abundance distribution that (approximately) best fits the observed abundances (*solid lines*).

star; more than 10 elements were detected in four stars, and more than five elements in an additional 13 stars. Employing typically 18 elements per star, Honda et al. (2004) have made fresh analyses of five of the stars studied by previous investigators and have added two additional ones. Barklem et al. (2005) have presented initial results of a halo-star survey specifically designed to identify and supply initial high-resolution abundance analyses of up to nine elements in new *n*-capture–rich candidates. Over 40 new *r*-process–rich stars were reported in that paper. More such stars will undoubtedly be discovered as the high-resolution survey work continues.

In all *r*-process–rich stars studied to date, the abundance distributions for the heavier *n*-capture elements ($Z \geq 56$, Ba and beyond) are nearly identical. We illustrate this apparently "standard" distribution in Figure 1 for five of these stars. The small star-to-star scatter in observed abundances about the mean pattern is dominated by observational/analytical uncertainties. This uniformity was probably not predictable a priori, since *n*-capture abundances in *r*-process–rich low-metallicity stars reflect contributions from a single supernova or a small number of supernova events, while the solar system (hereafter, SS) abundances result from many generations of supernovae. This suggests that there is a *unique* astrophysical site that dominates the nucleosynthesis of the heaviest *r*-process isotopes. The *r*-process mechanism for the synthesis of the $A \gtrsim 130$ isotopes (hereafter, the main component) must be extremely robust.

However, abundance patterns in the mass regime below $A \approx 130$ for the SS and very metal-poor stars do not support such a simple story. Considering data from carbonaceous chondrite meteorites, Wasserburg et al. (1996) first proposed that abundances of the short-lived ^{107}Pd and ^{129}I isotopes in primordial SS matter are inconsistent with their having been formed in uniform production together with the heavy *r*-process radioactivities (specifically, ^{182}Hf, ^{235}U, ^{238}U, and ^{232}Th). Wasserburg et al. argued that these two different mass ranges of nuclei require different timescales for production, and thus require two distinct *r*-process sites. Qian & Wasserburg (2000) further quantified this idea, distinguishing the two *r*-process occurrences as (1) H (high-frequency) events that are the main source of heavy *r*-process nuclei ($A > 130$), but not ^{129}I, and (2) L (low-frequency) events that are largely responsible for light *r*-process nuclei ($A < 130$) including ^{129}I. These suggestions formed the initial impetus for distinguishing so-called "weak" and "main" *r*-process components. We caution that this scenario is not universally accepted. For example, a pure *r*-process origin for the important ^{182}Hf abundance has been questioned by Meyer & Clayton (2000). Instead, those authors argue that the enhanced abundance of ^{182}Hf with respect to ^{107}Pd and ^{129}I in meteorites is due to the injection into the solar nebula of *s*-process material from outside the edge of the helium-exhausted core of a massive star. If this interpretation is valid, then one observational basis for two *r*-process sites may not be solid.

Inconsistencies between abundances of lighter and heavier *n*-capture abundances are also found in *r*-process–rich low-metallicity stars. If the SS *r*-process abundance curve is scaled to fit the metal-poor–star abundances of elements with $Z \geq 56$, then several elements in the range $39 \leq Z \leq 50$ (e.g., Y, Ag) appear to have significant underabundances in the stars. This result has been found in many of the studies cited above and is illustrated in detail in Figures 7 and 8 of Sneden et al. (2003). In addition, Johnson (2002), Aoki et al. (2005), and Barklem et al. (2005) have investigated the relationship between the abundances of the light Sr-Y-Zr group and the heavier main-component Ba in *r*-process–dominated stars, finding a very large scatter at lower metallicities. Travaglio et al. (2004) have explored the production of Sr-Y-Zr in relation to the heavier *n*-capture elements over a large stellar metallicity range. These results all provide further evidence for a second distinct (weak) *r*-process site for the synthesis of isotopes below $A \approx 130$.

In this paper we report updated theoretical *r*-process computations employing new nuclear data and use them to explore several aspects of SS and low-metallicity observational results of *n*-capture elements. The computations are described in § 2. The calculated *r*-process abundances are compared with selected observational data in § 3 to address: (1) neutron density constraints imposed by barium isotopic and elemental abundances, (2) the contributions from the two *r*-processes to light *n*-capture abundances, and (3) a new connection between rare-earth and the heaviest stable elements. Finally, in § 4 we discuss the new calculations in terms of nuclear chronometers.

2. *r*-PROCESS NUCLEOSYNTHESIS CALCULATIONS

Our *r*-process calculations were performed under the conditions of the waiting-point assumption or $(n,\gamma) \rightleftharpoons (\gamma,n)$ equilibrium (see Kratz et al. 1988, 1993, 2005a; Kratz 2006; Thielemann et al. 1994; Pfeiffer et al. 1997, 2001; Freiburghaus et al. 1999a). Although dynamic *r*-process calculations are feasible today (see, e.g., Freiburghaus et al. 1999a; Farouqi et al. 2006), the classical *r*-process approach can be employed to compare with the astronomical observations, the goal of this paper. Even with the simplistic assumptions of constant neutron number density and temperature and instantaneous freezeout, the equilibrium models presented here reproduce the SS abundances well. The classical approach is also largely independent of a stellar model, whereas all recent "more realistic" calculations imply a specific astrophysical environment, e.g., supernovae or neutron-star mergers, which may require quite different astrophysical parameter sets.

More recent large-scale, fully dynamic network calculations within the SN II high-entropy wind model have shown (Wanajo et al. 2004; Farouqi et al. 2005) that there exists a rather wide

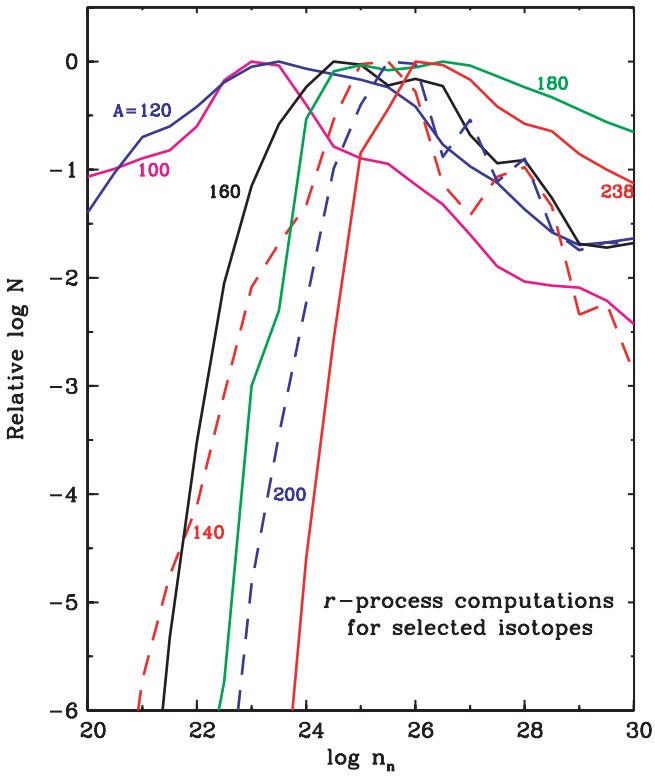

FIG. 2.—Representative *r*-process isotopic abundance predictions as a function of individual neutron number density n_n. The purpose of this figure is to show the relative efficiency of the *r*-process in producing various *n*-capture masses as n_n increases. Therefore, for display purposes here, the distribution for each isotope has been divided by its maximum value, so that all curves peak at normalized $\log N \equiv 0.0$, where N is a number density abundance.

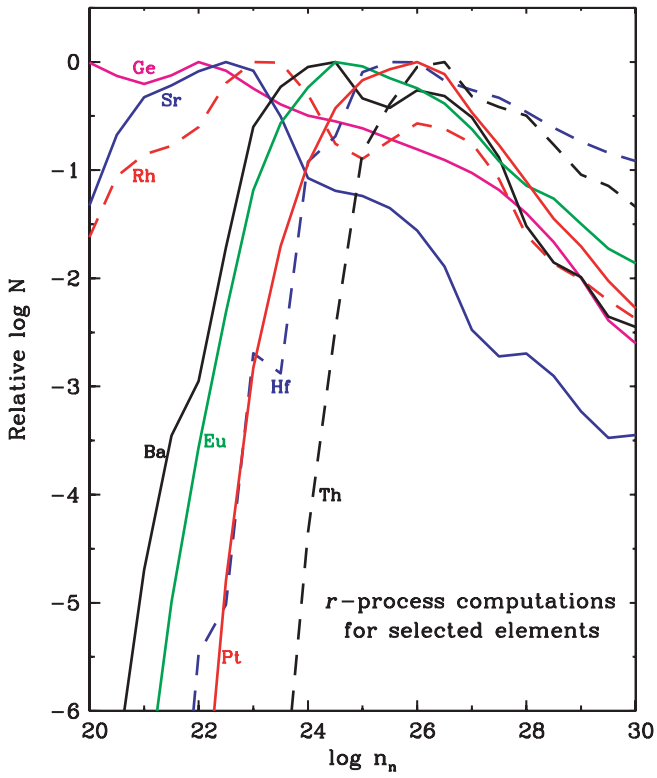

FIG. 3.—Representative *r*-process elemental abundance predictions as a function of individual neutron number density n_n. The distribution for each element has been divided by its maximum value, so that all curves peak at normalized $\log N \equiv 0.0$.

range of correlated astrophysical parameters, such as Y_e, S, Y_n, $Y_{\rm seed}$, and $V_{\rm exp}$, within which a robust *r*-process can be performed. However, so far SN models do not yet provide convincingly "unique" astrophysical conditions within the expected *r*-process parameter space, which would constrain the *r*-process. In addition, a careful comparison between the classical *r*-process (e.g., Kratz et al. 1993) with supernova thermodynamic trajectories given by Takahashi et al. (1994) has shown very good agreement (for T_9–n_n) between the "waiting-point" equilibrium and dynamic conditions. The assumption of constant n_n and temperature is also a good approximation up until the freezeout, as shown by, e.g., Freiburghaus et al. (1999a) and Farouqi et al. (2006). We also note that the neutron freezeout, which occurs on a very rapid timescale (Kratz et al. 1993), does not affect the abundances up to and slightly beyond the second peak and does not have a significant effect on the rare-earth or third *r*-process–peak regions (see, e.g., Rauscher 2004; Farouqi et al. 2006).

Our calculations to reproduce the total isotopic SS *r*-process abundance pattern covered a neutron-density range of $20 \leq \log n_n \leq 30$ in steps of 0.5 dex, with the neutron exposure times $\tau(n_n)$ and weighting functions $\omega(n_n)$ for each n_n-component as given in Kratz et al. (1993) and Cowan et al. (1999). The upper neutron-density limit is constrained by SS abundances. Our results indicate that the highest neutron number densities, $\log n_n \geq 30$, make little contribution to the overall abundances, a result that is confirmed by more detailed network calculations (e.g., Farouqi et al. 2006). More discussion of the astrophysical parameter choices is given in § 2.2. Predicted isotopic abundance trends with neutron density are displayed in Figure 2. The general shapes of the curves are the same for all isotopes, first, a generally sharp rise to a maximum, followed by a more gradual decline; if $\log n_n < 20$ abundance runs were to be displayed in Figure 2, then the rising portions of the curves would be more apparent for the lightest isotopes ($A = 100$ and 120). The details of the curves are dependent on individual nuclear properties and are discussed further.

Of greater interest for this paper are *n*-capture elemental abundances in metal-poor stars. Therefore, as stellar spectroscopy normally can yield only elemental abundances, in Figure 3 we show some examples of the *r*-process results summed by element. As in Figure 2, predicted abundances are plotted as a function of individual neutron number density $\log n_n$. Unsurprisingly, these elemental abundance variations are similar to the isotopic ones, and the same statement about the "missing" parts of the light isotope trends applies to the elemental curves as well. The data of these figures show that lighter *n*-capture elements are produced in bulk at smaller values of $\log n_n$ than are the heavier ones.

2.1. *Nuclear Data Input*

The best agreement with SS *r*-process abundances is obtained when we employ (1) the nuclear mass predictions from an extended Thomas-Fermi model with quenched shell effects far from stability (i.e., ETFSI-Q; Pearson et al. 1996) and (2) the β-decay properties from QRPA calculations for the Gamow-Teller (GT) transitions based on the methods described in Möller & Randrup (1990; see also Möller et al. 1997) and the first-forbidden strength contributions from the Gross theory of β-decay (Möller et al. 2003).

We have previously tested quite a number of global mass models in our classical *r*-process calculations (see, e.g., Kratz et al. 1998, 2000, 2005a, 2005b; Pfeiffer et al. 1997, 2001; Kratz 2006).

For our present paper we have chosen to use the "quenched" mass formula ETFSI-Q for the following reasons. In principle, a weakening of the strong $N = 82$ shell below ^{132}Sn had already been suggested by Kratz et al. (1993) from, at that time, scarce experimental indications in the phase transitional region around $A = 100$. Following the microscopic, self-consistent description of "shell quenching" far from stability in the spherical mass model HFB (Hartree-Fock-Bogoliubov)/SKP (Skyrme force) of Dobaczewski et al. (1996), Pearson et al. (1996) implemented this behavior in an algebraic procedure for the shell closures $N = 50$, 82, and 126 into their "unquenched" deformed ETFSI mass formula, hereafter called ETFSI-Q. The big improvement in changing the *r*-process matter flow at the closed-shell "bottlenecks," and consequently in reproducing the overall SS *r*-process abundance pattern by our classical waiting-point calculations, was evident immediately (Kratz et al. 1998; Pfeiffer et al. 1997, 2001).

Today, several other microscopic HFB models have become available with the same overall quality as the ETFSI-Q approach in terms of the rms differences between experimentally known and predicted masses (see, e.g., Lunney et al. 2003; Rikovska-Stone 2005; Pearson 2004). However, these models do not reproduce well the experimental $N = 82$ shell-gap behavior around double-magic ^{132}Sn, where the dominant bottleneck in the total *r*-process matter flow occurs (Kratz et al. 2005a, 2005b; Kratz 2006, and further discussion below). Furthermore, the recent HFB models show a rather unphysical chaotic behavior in their S_{2n} systematics, indicating that the treatment of pairing in these approaches is inadequate (see, e.g., Rikovska-Stone 2005, Kratz et al. 2005a, 2005b; Kratz 2006). To summarize, although ETFSI-Q may not be the ultimate mass model for *r*-process calculations, it is preferred for our computations because it best reproduces the experimentally measured nuclear-structure quantities of more than 20 *r*-process isotopes in the $A = 130$ *r*-abundance peak region.

Our nuclear database has been improved by including recent experimental results and, based on a better understanding of the underlying shell structure, new theoretical predictions. By now, altogether more than 50 isotopes lying in the *r*-process path under $\log n_n = 20$ freezeout conditions between ^{68}Fe and ^{139}Sb have been measured, at least via their β-decay half-life. Of particular importance are the new spectroscopic data on $N \simeq 82$ Ag, Cd, In, Sn, and Sb isotopes, which have led to a better understanding of the $A \simeq 130$ *r*-abundance peak as the major bottleneck for the *r*-process matter flow to the heavier elements (see, e.g., Kratz et al. 2000, 2005a, 2005b; Kratz 2006). In this context, presumably the measurement of utmost importance is the determination of the high (energy involved in a β-decay) Q_β value of $N = 82$ ^{130}Cd, which represents the isobaric mass difference between ^{130}Cd and its daughter ^{130}In (Dillmann et al. 2003; Kratz et al. 2005b). This experimental value is in clear disagreement with predictions from all older "unquenched" global mass models (e.g., GTNM [Gross Theory of Nuclear Masses], Hilf et al. 1976; FRDM [Finite Range Droplet Model], Möller et al. 1995; ETFSI-1, Aboussir et al. 1995), as well as from the recent series of more microscopic HFB approaches (e.g., HFB-2, Goriely et al. 2001; HFB-8, Samyn et al. 2004; HFB-9, Goriely et al. 2005; Rikovska-Stone 2005). The experimental value is only in agreement with the "quenched" mass models HFB/SKP (Dobaczewski et al. 1996), ETFSI-Q (Pearson et al. 1996), and the latest nuclear-mass evaluation of Audi et al. (2003).

An analysis of the discrepancies between measured and calculated β-decay properties reveals considerable improvement over the earlier evaluation. For potential *r*-process progenitor isotopes with half-life $T_{1/2} \leq 0.2$ s, the total error is now a factor of 2; for the β-delayed neutron emission probability, $P_n \geq 1\%$, the mean deviation is a factor of 3. Moreover, we have performed a careful parameter study of the "robustness" of $T_{1/2}$ and P_n predictions of the $N \simeq 126$ waiting-point nuclei forming the $A \simeq 195$ *r*-process peak, where no experimental data are available at all. Again, our model predictions lie within a factor of 2 of the observed abundances; this is in contrast to earlier calculations, often uncertain by an order of magnitude or more, that were dominated by uncertain nuclear physics data for the most neutron-rich nuclei. Taken together, this gives us confidence in the reliability of our nuclear physics input to the subsequent *r*-process calculations.

2.2. *Abundance Fits to the Sun and CS 22892−052*

As our calculations demonstrate, a range of neutron densities are required to reproduce all major features of the SS meteoritic *r*-process isotopic abundance distribution. However, we remind the reader that the *total* meteoritic abundances are generally combinations of both *s*-process and *r*-process contributions. Because the *s*-process proceeds along the valley of stability and depends mostly on neutron capture cross sections that are directly measurable in the lab, its fraction of the total can be estimated. This is done either empirically by fitting a smooth curve to the $N\sigma$ versus mass distribution of isotopes that can only be synthesized in the *s*-process (Käppeler et al. 1989; Burris et al. 2000; Simmerer et al. 2004; Cowan et al. 2006), or theoretically by computing an abundance set with conditions that correspond to those expected in stellar interior He-fusion zones (Arlandini et al. 1999; Travaglio et al. 2004). Then the chosen *s*-process abundance set is subtracted from the total SS abundances to yield the *r*-process set. The resulting *r*-process abundances may be very accurate for those isotopes with little *s*-process contribution (e.g., ^{151}Eu and ^{153}Eu), but have significant uncertainties for isotopes where the *s*-process fraction is dominant (e.g., ^{138}Ba, the most abundant of the seven naturally occurring Ba isotopes). This caution should be kept in mind in all SS *r*-process abundance comparisons, but see also a recent attempt at directly predicting the SS *r*-process abundances for several rare-earth elements (Den Hartog et al. 2006).

Attempts to fit predicted *r*-process abundances to the SS values require assumption of a continuous addition of a small number of individual neutron density components, with a varying *r*-process path related to contour lines of constant neutron separation energies in the range of 4–2 MeV (the latter being determined by the combination of neutron number density and temperature). The number of such components needs to be at least four to match the relative abundances of the three *r*-process abundance peaks ($A = 80$, 130, and 195) and abundances in the actinide region (Kratz et al. 1993). Less than 20 components are sufficient to match the detailed *r*-process SS abundances (Pfeiffer et al. 1997; Cowan et al. 1999). Adding more components produces no further improvement, given the present uncertainties in both *r*-process computations and *r*-process SS abundances.

While such a procedure is both largely site independent and mainly intended to produce a good fit to solar *r*-process abundances, it can also provide information regarding the conditions that a "real" *r*-process site must fulfill. The fit is performed by adjusting the weight of the individual components [or different neutron separation energies $S_n(n_n, T)$] and the time duration τ for which these (constant) conditions are experienced, starting with an initial abundance in the Fe group.[7] For a given (arbitrary) temperature, S_n is a function of neutron number density n_n. The addition weights $\omega(n_n)$ and process durations $\tau(n_n)$ have a

[7] We have also performed computations that employ a "Zr seed" beyond $Z = 40$, $N = 50$, and the results are similar.

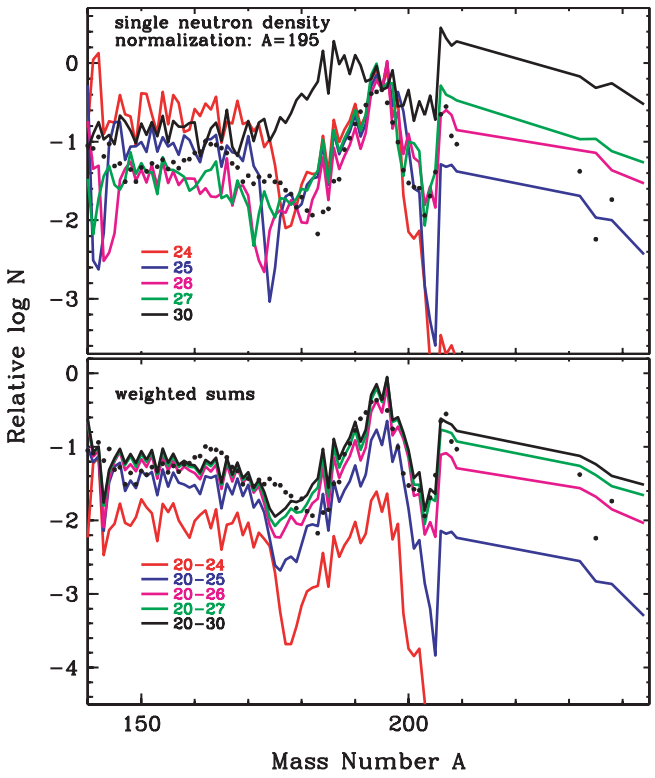

FIG. 4.—Relationship between component abundances computed at single neutron densities and their weighted sums. *Top*: Solid curves representing single neutron densities chosen in the range $\log n_n = 24$ to 30, and circles representing solar isotopic abundances. The curves are shifted to agree with the solar value at $A = 195$. *Bottom*: Sums of the individual components weighted by the form $\omega(n_n) \simeq 8.36 \times 10^6 n_n^{-0.247}$.

behavior similar to powers of n_n. This corresponds to a linear relation in $\log n_n$ and is already observed when taking a minimum of three components in order to fit the *r*-process abundance peaks (Kratz et al. 1993; Cowan et al. 1999). This approach (although only a fit and not a realistic site calculation) is reasonable to the extent that such a continuous dependence on physical conditions can be expected to reflect the range of conditions appropriate to the (yet unidentified) astrophysical site.

The effect of the weighting of the sums of the various components on the abundance fit is shown in the bottom panel of Figure 4. Relatively small weighting factors for the highest neutron number densities and larger weighting values for lighter neutron density components yield good fits to the data. Overall the best fit to this region of the SS abundances (from $A \approx 130$ to the actinides) is that of $\log n_n = 20$ to 26–27.

For a choice of a typical freezeout temperature (in billions kelvin) of $T_9 = 1.35$ (see, e.g., Cowan et al. 1999), the necessary addition of components (with *r*-process paths of a corresponding neutron separation energy S_n over a duration τ) can be expressed in the form $\omega(n_n) \simeq 8.36 \times 10^6 n_n^{-0.247}$ and $\tau(n_n) = 6.97 \times 10^{-2} n_n^{0.062}$ s. This algebraic/exponential fit is in good agreement with full network calculations (Farouqi et al. 2006) for the high-entropy wind scenario in terms of *r*-process seed nuclei as a function of entropy/neutron density. When restricting the fit to the mass regions around the *r*-process peaks ($A \simeq 80$, 130, and 195), where the paths come closest to stability, model extrapolations need not be extended far into unknown territory. Even a significant amount of experimental information is available (Pfeiffer et al. 2002; Audi et al. 2003; Kratz et al. 2005a; Kratz 2006), and is now being used in the calculations. These power laws in n_n play roles comparable to that of the assumed exponential addition of neutron exposures in the classical *s*-process.

The relationship between component abundances computed at single neutron densities to their superposition is illustrated in Figure 4. In the top panel we show individual, unweighted calculations, ranging from $\log n_n = 24$ to 30, superimposed on the solar isotopic abundances (*black dots*). We have arbitrarily normalized all curves to match the abundances at $A = 195$. There are several trends evident in this plot. First, larger neutron number densities ($\log n_n \geq 25$), in general, are required to synthesize the heaviest elements (i.e., the third peak and actinide regions). The larger values of n_n are needed to push the so-called "*r*-process path," defining where these nuclei are produced, far enough away from stability and to very neutron-rich regions, so that the synthesized radioactive nuclei subsequently decay back to high enough mass numbers (e.g., see Fig. 1 in Cowan & Thielemann 2004). However, the highest neutron density ($\log n_n = 30$) overproduces the heavy region and the Eu region ($A \approx 150$). In addition, the largest neutron densities produce ratios of third peak to interpeak abundances that are clearly different than those observed in the SS. This occurs because such a high value of n_n pushes the *r*-process path too far into the neutron-rich region and consequently overproduces the heaviest nuclei. On the other hand, the lighter neutron number densities $\log n_n = 24$ do mimic the $A \approx 150$ range, but are clearly inadequate to synthesize the third peak abundances. This reinforces the idea that multiple neutron exposures are required to reproduce the three different SS peaks; one exposure will not be adequate.

We show in Figure 5 the detailed steps in one such typical *r*-process addition calculation. These calculations include explicitly β-decays back to pseudostability (i.e., with a long half-life), but do not include α-decays from the translead region. In the top panel of this figure, the summation of five individual neutron number density components in the range $\log n_n = 20$–22 have been tuned to reproduce the $A = 80$–100 SS isotopic *r*-process abundances. This composition is clearly inadequate to reproduce the abundances of the heavier isotopes. As shown in the second panel of Figure 5, addition of higher neutron number density components (up to $\log n_n = 24$) mostly reproduces the $A = 130$ *r*-process abundance peak. Therefore, we estimate that the division between weak and main *r*-process density regimes occurs at $\log n_n \simeq 23.0 \pm 0.5$. Likewise, to form the heaviest stable elements, the third *r*-process peak, it is necessary to include neutron number density components at least up to $\log n_n \simeq 26$ (Fig. 5, *third panel*). However, even this neutron density is still insufficient to reproduce the abundances of the translead region (including Th and U), which requires $\log n_n \simeq 28$ as shown in the bottom panel of the figure.

In Figure 6 the illustration is reversed. Considering our best-fit weighted *r*-process distribution (the bottom panels of both Figs. 5 and 6) leads to a few comments. First, the *r*-process parts of the heaviest stable elements Pb ($Z = 82$, $A = 206$–208) and Bi ($Z = 83$, $A = 209$) in the SS are principally due to α-decays of nuclei along the radioactive decay chains extending through the actinide region. Their observed abundances are reproduced well by our calculations. We show in the subsequent panels (starting at the top with the highest values only) how progressively adding additional lower neutron number density components leads to a better and better fit of the SS isotopic abundances; specifically, in the second panel at the rare-earth region, in the third panel for the $A = 195$ peak, and in the bottom panel for the complete SS abundance pattern (see Cowan et al. 1999). We note also, as illustrated in Figure 5, that very low neutron densities ($\log n_n \simeq 20$) are insufficient to reproduce the first *r*-process peak, and very high

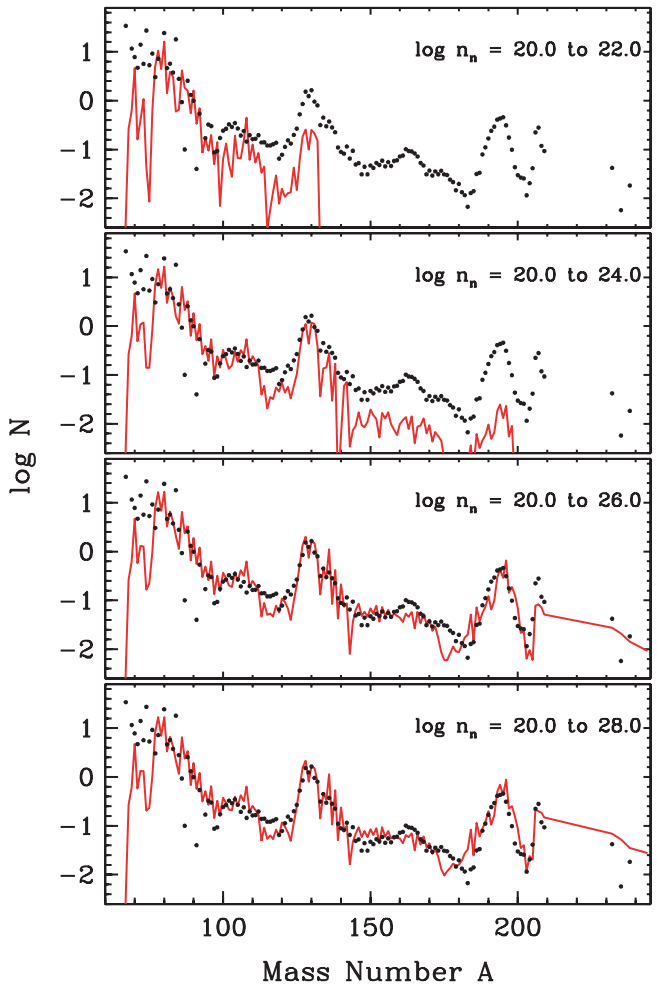

FIG. 5.—Comparison of meteoritic SS *r*-process–only isotopic abundances to weighted sums of *r*-process computations for different neutron densities ranges. The SS abundances (*black points*; Käppeler et al. 1989; Wisshak et al. 1998; O'Brien et al. 2003; see listing in Cowan et al. 2006) are on the standard meteoritic scale in which $\log N_{\rm Si} = 6$. The four panels show from top to bottom the effect of incorporating progressively higher ranges of n_n. The top panel predictions span $20.0 \leq \log n_n \leq 22.0$, adequate only for matching the lightest isotopes. The bottom three panels successively add more neutron density components weighted to simultaneously match the greatest mass range of nuclei. The values displayed here are ones taking into account α- and β-decays of nuclei back to stability.

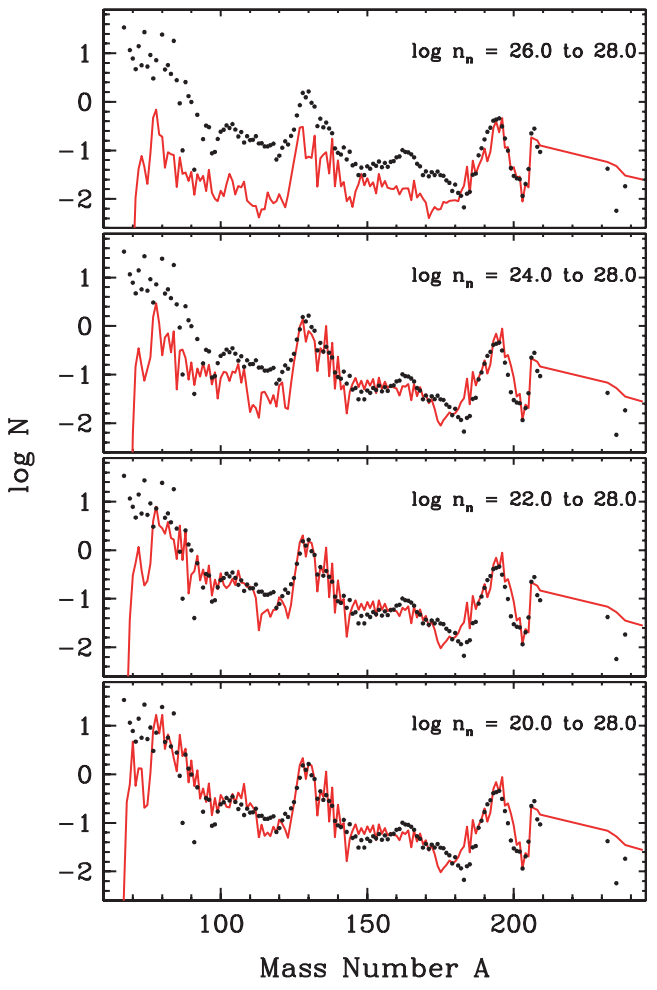

FIG. 6.—Another comparison of meteoritic *r*-process abundances and weighted sums of *r*-process computations. For this figure additions commence at the high-density end and progressively add components of lesser values of $\log n_n$ to fit the lighter *r*-process abundances. The symbols and lines are as in Fig. 5

densities ($\log n_n = 30$) overproduce the third peak and the actinides, as shown in Figure 4.

Summing the individual isotopic abundances into elemental abundances also reproduces the observed SS *r*-process *elemental* curve from $Z = 30$–82. Since, we and many other investigators (cited in § 1) have argued that the abundance pattern in *r*-process–rich metal-poor stars is also consistent with this SS distribution (Fig. 1), it is not surprising that multiple neutron density ranges are required to adequately match the entire *n*-capture abundance ranges of the stars as well.

As an example, we compare in Figure 7 the empirical SS *r*-process elemental distribution, theoretical *r*-process predictions, and abundances of the *r*-process–rich low-metallicity star CS 22892−052 (Sneden et al. 2003; with updated abundances of Nd, Sm, Gd, Hf, and Pt as indicated in the figure caption). The SS distribution has been scaled to match the CS 22892−052 Eu abundance. In the top panel of Figure 7, the main *r*-process abundance calculations, for $\log n_n \geq 23.0$, have also been normalized at the stellar Eu abundance. Good agreement is seen between the calculations and the mean observed abundance levels for stable *n*-capture elements throughout the range $56 \leq Z \leq 82$. Comparing the CS 22892−052 and the scaled solar abundances (for $Z = 56$–82), we find an average difference of $\langle (\text{CS 22892}-052) - \text{SS}_{r\text{-only}} \rangle = 0.044$ and $\sigma = 0.096$. The comparison between the stellar and our calculated *r*-process abundances yields $\langle (\text{CS 22892} - 052) - (\text{main } r\text{-process theory}) \rangle = 0.15$ and $\sigma = 0.25$. The main *r*-process as defined here reproduces the CS 22892−052 data of the heavier elements ($Z > 56$), including the full $A = 130$ second *r*-process peak, including iodine. However, both the SS *r*-process–only curve and our calculations (for the main *r*-process) do not fit the lighter *n*-capture element data ($Z < 56$) in this star. In particular Y, Mo, Pd, and Ag all deviate from both of these curves. These differences in fact have been one of the main supports for the existence of two *r*-processes. We note, however, that the main *r*-process calculations reproduce the odd-*Z*, even-*Z* abundance staggering in both light and heavy *n*-capture elements in CS 22892−052. Furthermore, the calculated abundances fall off significantly with respect to the SS *r*-only abundances at the lower atomic numbers and do not seriously clash with the four abundances for which only upper limits have been determined: Ge, Ga, Cd, and Sn.

Elemental abundance predictions of the weak *r*-process ($\log n_n < 23$) are overlaid with the observed abundances of CS 22892−052 in the bottom panel of Figure 7. These predictions only represent the light "missing part" of the solar *r*-process

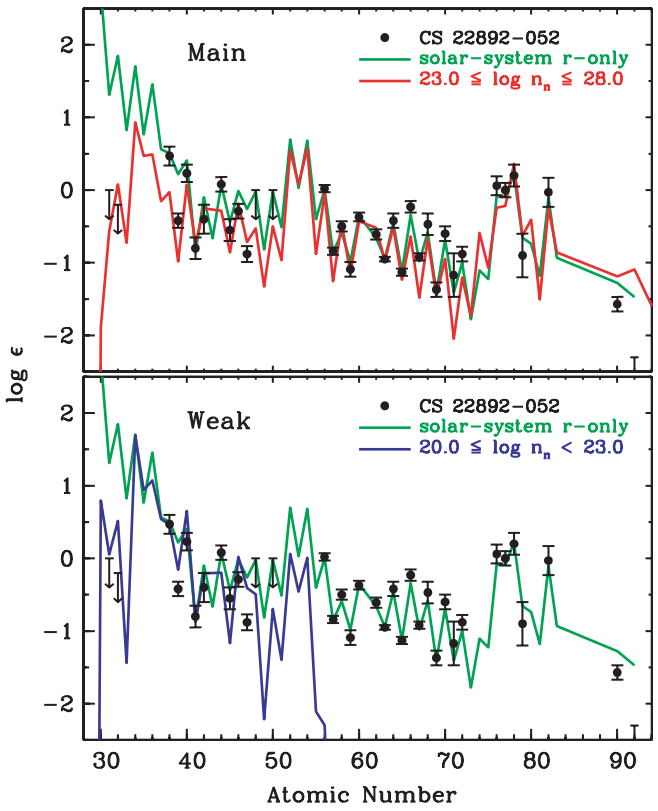

FIG. 7.—Abundances of *n*-capture elements in CS 22892−052 compared with *r*-process distributions. In both panels the filled circles are the CS 22892−052 data, mostly from Sneden et al. (2003), with some updated abundances based on recent transition probability studies: Nd (Den Hartog et al. 2003), Sm (Lawler et al. 2006), Gd (Den Hartog et al. 2006), Hf (Lawler et al. 2007), and Pt (Den Hartog et al. 2005). Upper limits are shown as downward-pointing arrows. In both panels the SS *r*-process elemental abundances (Simmerer et al. 2004), scaled to match the CS 22892−052 Eu value, are indicated by green lines. In the top panel the main *r*-process predictions (neutron number densities $\log n_n \geq 23$) summed by element are shown with a red line and normalized to the stellar Eu abundance. In the bottom panel, predictions for the weak *r*-process are shown with a blue line where the scaling is approximate for illustration purposes.

abundances (similar to that of Fig. 5, *top*). The scaling to the CS 22892−052 light *n*-capture abundances is approximate and for display purposes only. Consistency between predicted and observed abundances of these elements can be achieved under the weak *r*-process conditions with little production of the heavier elements (5%−10% of the second *r*-process peak and essentially 0% for Ba and beyond). As can be seen in the figure, the weak *r*-process predictions do not contribute to the heavier ($Z > 56$) *n*-capture element abundances. In other words the similar *r*-process abundance pattern (for the elements with $Z \geq 56$) seen in the *r*-process–rich metal-poor stars (Fig. 1) does not need or have any contribution from the weak *r*-process. The figure also confirms our results from above, that the first SS *r*-process abundance peak can be reproduced with a low n_n ($<10^{23}$).

The general conclusions about a separation in abundance levels (and the associated synthesis conditions) between the lighter and heavier *n*-capture elements are not new, and have been discussed previously in the literature (e.g., Sneden et al. 2003; Ivans et al. 2006; Cowan & Sneden 2006). However, our new calculations suggest that the separation occurs below the element iodine, which appears to be formed along with Ba in the $A = 130$ abundance peak. We note in this regard that there are experimental nuclear data in the *r*-process path in the mass range from ^{68}Fe to ^{140}Te. For these isotopes where the *s*-process data might not be well defined (leading to large uncertainties in the *r*-process residuals), the experimental *r*-process data might be used in the future to directly predict, or at least constrain, the actual SS *r*-process abundances. Such data could be employed to quantify where in mass (atomic number) the possible separation between the main and weak *r*-process (if one exists) occurs.

3. DETAILED ABUNDANCE SIGNATURES OF THE *r*-PROCESS

In this section we consider some additional *r*-process abundance clues from the details of our calculations, beyond considerations of the overall fits to solar and stellar abundance distributions. In the near future some isotopic, as well as additional (yet unobserved) elemental, abundance ratios will become available for certain stars. Such ratios will provide increasingly stringent constraints on both *s*- and *r*-process nucleosynthesis contributions. Our calculations predict isotopic abundance ratios for the light-heavy elements, up to the heavy wing of the $A = 130$ peak, which includes, for example, the Ba isotopes. At least within the high-entropy model, the freezeout is very fast; nonequilibrium captures do not play a significant role; P_n values are small (Kratz et al. 1993; Freiburghaus et al. 1999a; Rauscher 2004; Farouqi et al. 2006). Hence, the final abundance pattern of the *whole* $A = 130$ peak, including the Ba isotopes, is mainly determined by the initial "progenitor abundances" with their odd-*Z*/even-*Z* staggering smoothed out by delayed neutron emission during the decay back to stability. These calculations should not be viewed as necessarily tightly constraining those isotopic ratios, but instead predicting a reliable range of values as a function of neutron number densities or entropy.

3.1. *Barium Isotopic Fractions*

An additional probe of the heavy element pattern and its range in metal-poor stars is provided by the (limited) isotopic abundance information that has been reported in the literature. The isotopes of Eu in metal-poor halo stars have been investigated by Sneden et al. (2002) and Aoki et al. (2003a, 2003b). For several *r*-process–rich stars, the isotopic abundance fraction ratios, $f(^{151}\mathrm{Eu})/f(^{153}\mathrm{Eu}) = N(^{151}\mathrm{Eu})/N(^{153}\mathrm{Eu}) = 1.0 \pm 0.1$, are in good agreement with the meteoritic *r*-process fraction, $f(^{151}\mathrm{Eu})/f(^{153}\mathrm{Eu}) = 0.478/0.522 = 0.916$ (Anders & Grevesse 1989). Estimates of the photospheric Eu isotopic ratio (Hauge 1972; Lawler et al. 2001) are also in accord with these values.

Barium has five naturally occurring isotopes, $A = 134$–138, which are produced in substantially different amounts in the *s*- and *r*-process.[8] Even-*Z* isotopes ^{134}Ba and ^{136}Ba cannot be reached by the *r*-process. As a result the abundance ratio of odd-*A* isotopes to the total, defined as $f_{\mathrm{odd}} \equiv [N(^{135}\mathrm{Ba}) + N(^{137}\mathrm{Ba})]/N(\mathrm{Ba})$, is larger in *r*-process than *s*-process nucleosynthesis events; $f^r_{\mathrm{odd}} > f^s_{\mathrm{odd}}$. In principle, observation should be able to assess f_{odd} in stars, for the odd-*Z* isotopes ^{135}Ba and ^{137}Ba have hyperfine-split line substructures that the even-*Z* isotopes lack. Therefore, careful measurement of the line broadening of Ba II lines should indicate the relative *r*-/*s*-process contributions to Ba production.

Unfortunately even the SS value of f^r_{odd} for Ba, which can be determined from meteoritic studies, is not known to high accuracy. This stems from the overall *s*-process dominance of barium in SS material. The *r*-process contributions to the barium isotopes are small, thus any isotopic abundance uncertainties are magnified in the estimates of their *r*-process contributions. Lodders (2003)

[8] Two other very minor but stable isotopes, ^{130}Ba and ^{132}Ba, are products of the *p*-process and not relevant to the present study.

TABLE 1
r-Process Isotopic Barium Abundances

log n_n	^{134}Ba	^{135}Ba	^{136}Ba	^{137}Ba	^{138}Ba	f_{odd}[a]
20.0.....	...	1.40E−09	...	1.71E−11	1.32E−10	9.15E−001
20.5.....	...	5.96E−08	...	4.00E−10	3.19E−09	9.49E−001
21.0.....	...	3.88E−06	...	3.27E−09	2.63E−08	9.93E−001
21.5.....	...	6.70E−05	...	1.62E−07	7.90E−07	9.88E−001
22.0.....	...	1.04E−04	...	1.76E−05	9.45E−05	5.62E−001
22.5.....	...	8.65E−04	...	4.32E−04	2.43E−03	3.48E−001
23.0.....	...	1.96E−02	...	4.31E−03	2.45E−02	4.94E−001
23.0.....	...	1.96E−02	...	4.31E−03	2.45E−02	4.94E−001
23.5.....	...	4.93E−02	...	9.63E−03	5.50E−02	5.17E−001
24.0.....	...	7.25E−02	...	1.54E−02	8.64E−02	5.04E−001
24.5.....	...	6.35E−02	...	2.12E−02	1.09E−01	4.38E−001
25.0.....	...	2.60E−02	...	1.30E−02	5.00E−02	4.38E−001
25.5.....	...	3.02E−02	...	9.39E−03	3.32E−02	5.44E−001
26.0.....	...	3.80E−02	...	1.13E−02	5.62E−02	4.68E−001
26.5.....	...	2.76E−02	...	1.04E−02	5.59E−02	4.05E−001
27.0.....	...	1.02E−02	...	7.63E−03	4.16E−02	3.00E−001
27.5.....	...	3.42E−03	...	3.38E−03	1.85E−02	2.68E−001
28.0.....	...	2.36E−03	...	5.50E−04	2.98E−03	4.95E−001
28.5.....	...	1.52E−03	...	2.90E−04	9.01E−04	6.68E−001
29.0.....	...	6.99E−04	...	2.95E−04	9.83E−04	5.03E−001
29.5.....	...	5.98E−04	...	4.32E−05	2.15E−04	7.48E−001
30.0.....	...	4.69E−04	...	5.14E−05	1.67E−04	7.56E−001

[a] Here $f_{odd} \equiv [N(^{135}\mathrm{Ba}) + N(^{137}\mathrm{Ba})]/N(\mathrm{Ba})$.

has given a new empirical estimate of the *r*-process and *s*-process contributions to each barium isotope, and with those data we compute a value of $f^r_{odd} = 0.72$. The Lodders isotopic breakdowns are very similar to those that were used by Burris et al. (2000) and Simmerer et al. (2004) to compute total solar elemental abundances of *n*-capture elements (see also the isotopic breakdowns in Cowan et al. 2006). Arlandini et al. (1999) subtracted *s*-process model calculations from the solar isotopic abundances to yield their *r*-process contributions. From their data we compute $f^r_{odd} = 0.46$.

These independent assessments of f^r_{odd} for Ba in the SS are in agreement mainly because the uncertainties in each are large, about ±0.2. Lacking a clear indication of which value to adopt, we simply average them to adopt $f^r_{odd} \approx 0.60 \pm 0.20$. In contrast, f^s_{odd} is tightly constrained between values of 0.09 and 0.11 in all of the estimates, but this again is due to the *s*-process dominance of Ba synthesis in SS material. From these independent assessments we adopt $f^s_{odd} = 0.10 \pm 0.02$.

In Table 1 we list our theoretical *r*-process predictions for Ba isotopic abundances and the resulting f^r_{odd} values. These calculations are for single fixed neutron number density conditions for $20 < \log n_n < 30$. We show the trend of f^r_{odd} with neutron number density in Figure 8, also indicating in the figure the SS values of f^r_{odd} and f^s_{odd}. In addition to the theoretical calculations adopted here, some full dynamic network calculations have been performed (Farouqi et al. 2006) in the context of the high-entropy supernova model, with post processing during the nonequilibrium neutron-freezeout phase. These computations have been made to check or constrain the more simplistic, but detailed, parametric predictions from the waiting-point approximation employed here. The Farouqi et al. calculations employ an extension of the dynamic *r*-process code (Freiburghaus et al. 1999a; Cowan et al. 1991), but include *n*-capture cross sections from the NON-SMOKER code (Rauscher & Thielemann 2000). For a range of conditions (electron abundance Y_e from 0.41 to 0.49, entropy S of 200–300 k_b baryon^{-1}) these dynamic calculations predict a range of f^r_{odd}

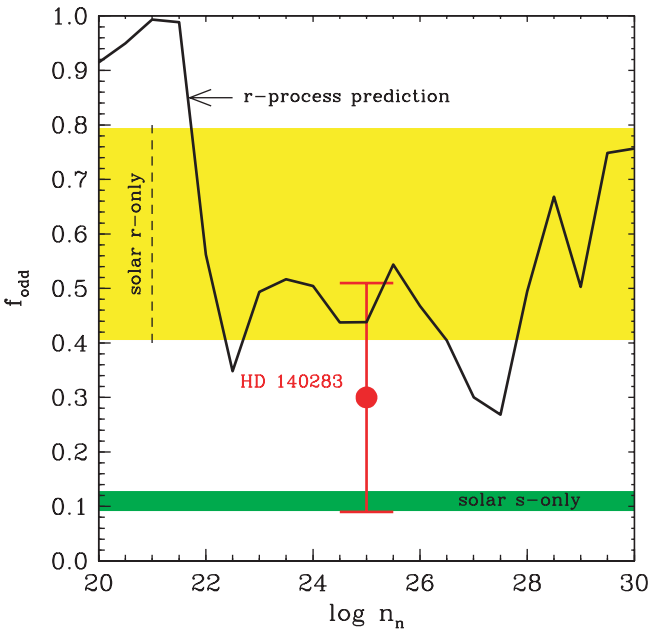

Fig. 8.—Predicted *r*-process barium odd-*Z* abundance fractions, $f^r_{odd} = [N(^{135}\mathrm{Ba}) + N(^{137}\mathrm{Ba})]/N(\mathrm{Ba})$, plotted vs. neutron number density. In addition to the black solid curve representing the predicted values, we have drawn a red solid circle with error bar to indicate the observed $f_{odd} = 0.30 \pm 0.21$ in the very metal-poor halo star HD 140283 (Lambert & Allende Prieto 2002). This point has been arbitrarily placed at $\log n_n = 25$ for illustration in the figure, but only the vertical placement of the point has meaning here. Also shown is a yellow color band indicating the SS *r*-process–only $f^r_{odd} = 0.6 \pm 0.2$ range and a green band indicating the *s*-process–only value $f^s_{odd} = 0.11 \pm 0.02$ range.

values of 0.48–0.51, thus overlapping with the waiting-point approximation values.

Few assessments of f_{odd} in metal-poor stars have been attempted. The wavelength shifts due to isotopic mass differences and hyperfine splits for the two odd-*A* barium isotopes are comparable to the line widths (due to thermal and microturbulent broadening) in stellar spectra, making isotopic abundance determinations very challenging. Recently, Lambert & Allende Prieto (2002), following an earlier investigation by Magain (1995), observed the Ba II 4554 Å line in the halo subgiant HD 140283 ($[\mathrm{Fe/H}] = -2.4$), at very high spectral resolution and signal-to-noise ratio. Detectable excess breadth of this line compared with single-component absorption features would be due mainly to the hyperfine splitting of the odd-*A* isotopes. Lambert & Allende Prieto detected the excess broadening at a marginal level, and their line profile analysis yielded a combined fractional abundance of the odd-*A* isotopes $f_{odd} = 0.30 \pm 0.21$.

The HD 140283 result is shown in Figure 8. Within large uncertainties, $f_{odd}(\mathrm{HD\ 140283}) \sim f^r_{odd}$ (SS). Frustratingly, the range in isotopic values for HD 140283 does not permit exclusion of the SS *s*-process value. Given that the HD 140283 result is marginally more consistent with an *r*-process than an *s*-process origin for that star, we examine the implications of our *r*-process calculations. As indicated in Table 1 and Figure 8, the lowest neutron number densities, $\log n_n \lesssim 22$, produce very small amounts of Ba. Since these low densities also yield f^r_{odd} values at odds with SS values, they are excluded from consideration here. Likewise, the highest neutron number densities, $\log n_n > 28$, predict Ba isotopic fractions that are much larger than the values permitted by the HD 140283 measurement. Averaging the isotopic abundances in the range $23 \leq \log n_n \leq 28$ yields $f^r_{odd} = 0.44$, very similar to the Arlandini et al. (1999) value and that found from the preliminary

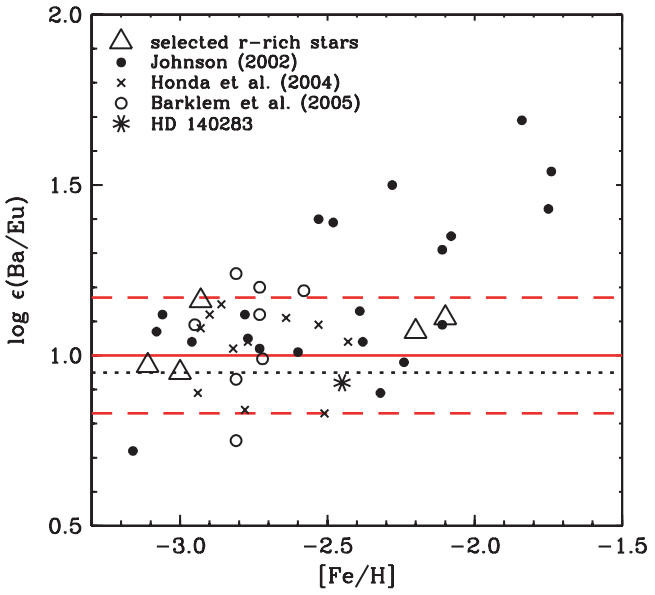

FIG. 9.—Observed barium-to-europium abundance ratios in metal-poor stars. The data shown here are representative of the recent literature, and their sources are given in the text. The black dotted line represents the solar *r*-process value of $\log \epsilon(\mathrm{Ba/Eu})$. The red solid line with the two red dashed lines indicate our best estimate of this ratio and its uncertainty in *r*-process–rich stars.

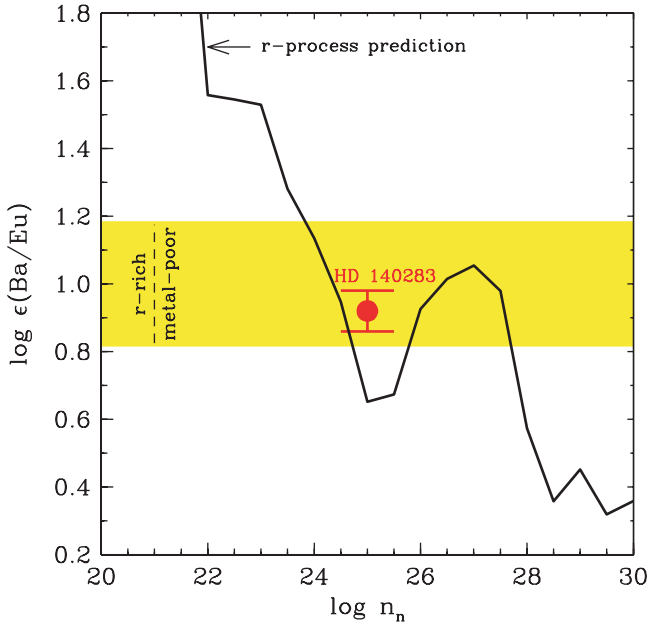

FIG. 10.—Predicted elemental abundance ratios $\log \epsilon(\mathrm{Ba/Eu})$ plotted vs. neutron number density $\log n_n$. The red point with error bar indicates the value derived for HD 140283 by Gratton & Sneden (1994). Also shown is a yellow band covering the $\log \epsilon(\mathrm{Ba/Eu})$ range reported in the literature for *r*-process–rich very metal-poor stars, as established in Fig. 9.

dynamic calculations. The meager Ba isotopic abundance data do not permit a more sharply defined neutron density range.

3.2. *Barium and Europium r-Process–rich Metal-deficient Stars*

More progress can be made by considering Ba/Eu elemental abundance ratios, which have been used for decades to estimate the relative influence of *s*-process and *r*-process contributions to stellar *n*-capture abundances (e.g., see Spite & Spite 1978). For SS material, $\log \epsilon_r(\mathrm{Ba}) = +1.446$ and $\log \epsilon_r(\mathrm{Eu}) = +0.494$, or $\log \epsilon_{r,\mathrm{SS}}(\mathrm{Ba/Eu}) = +0.952$. For HD 140283 Gratton & Sneden (1994) reported $[\mathrm{Ba/Fe}] = -0.64 \pm 0.06$ and $[\mathrm{Eu/Fe}] = +0.09 \pm 0.01$, yielding $[\mathrm{Ba/Fe}] = -0.73 \pm 0.06$, which translates to $\langle \log \epsilon_{\mathrm{obs}}(\mathrm{Ba/Eu}) \rangle = +0.92 \pm 0.06$ using their solar Ba and Eu abundances. This abundance ratio is obviously in good agreement with $\log \epsilon_{r,\mathrm{SS}}(\mathrm{Ba/Eu})$, strengthening the suggested attribution of $f_{\mathrm{odd}}(\mathrm{Ba})$ to an *r*-process–only synthesis.

Many very low metallicity stars exhibit similar Ba/Eu ratios. We surveyed the literature to estimate these spectroscopic values. In Figure 9 we plot [Ba/Eu] as a function of [Fe/H] from several recent halo-star comprehensive abundance analyses: Johnson (2002), Honda et al. (2004), and Barklem et al. (2005). We added points from detailed studies of a few extremely *n*-capture–rich stars (Westin et al. 2000; Cowan et al. 2002; Hill et al. 2002; Sneden et al. 2003; Ivans et al. 2006). This is a representative (but not complete) list of Ba/Eu abundance studies in this metallicity domain. A large majority of the stars considered in the cited studies exhibit $\langle \log \epsilon_{\mathrm{obs}}(\mathrm{Ba/Eu}) \rangle \simeq +1.00$. Some points scatter to significantly larger values ($\gtrsim$+1.4) of this quantity, clearly indicative of substantial *s*-process contributions to Ba in those stars. The envelope containing essentially the entire star-to-star scatter of the Ba/Eu ratios observed in *r*-process–rich stars is $\approx$0.35 in width, or $\langle \log \epsilon_{\mathrm{obs}}(\mathrm{Ba/Eu}) \rangle = +1.00 \pm 0.17$.

In Figure 10 we show our calculated Ba/Eu abundance ratios plotted as a function of neutron number density. To this figure we add a point representing the value for HD 140283 and a color band representing the range in values for *r*-process–rich low-metallicity stars. The neutron number density range containing theoretical predictions and stellar observations is substantially less than that inferred from consideration of Ba isotopic abundances alone. This figure, together with $\log \epsilon_{r,\mathrm{SS}}(\mathrm{Ba/Eu}) = +0.95$, suggests that $24 \lesssim \log n_n < 28$, with fairly well-defined boundaries on both ends of the allowable neutron number density range. Densities beyond this domain appear unable to reproduce $f_{\mathrm{odd}}(\mathrm{Ba})$ and $\log \epsilon(\mathrm{Ba/Eu})$ of metal-poor *r*-process–rich stars and, by extension, the relative abundances of most rare-earth elements in these stars.

3.3. *The Iodine–Barium Connection*

The existence of two distinct *r*-process synthesis sites began with the Wasserburg et al. (1996) critical assessment of ^{129}I and ^{182}Hf meteoritic abundance levels. In the preceding subsections we demonstrated that *r*-process computations with an addition of neutron densities in the range $24 \lesssim \log n_n < 28$ yield both barium isotopic and Ba/Eu elemental abundance ratios that are compatible with the solar *r*-process abundances.

Computed abundances of Sr ($Z = 38$), I (53), Hf (72), and Ba (56) are shown in the top panel of Figure 11, and several abundance ratios among these elements are shown in the bottom panel. These are plotted as a function of the neutron density range defined in the following way. Beginning at the highest neutron density $\log n_n = 30$, successively smaller neutron density steps represent the accumulation of the weighted abundances resulting from that particular neutron density *plus* the total of all higher densities. The highest values of $\log n_n$ contribute only trace amounts of the solar and stellar *r*-process abundances, which then grow as smaller neutron density contributions are added into the sums. The abundance curve of the heavy element Hf "saturates" at its approximate solar value most quickly (at $\log n_n \simeq 25.5$), in agreement with the overall trend shown in Figure 6, while the light element Sr does not reach its SS *r*-process value until $\log n_n \simeq 21.5$.

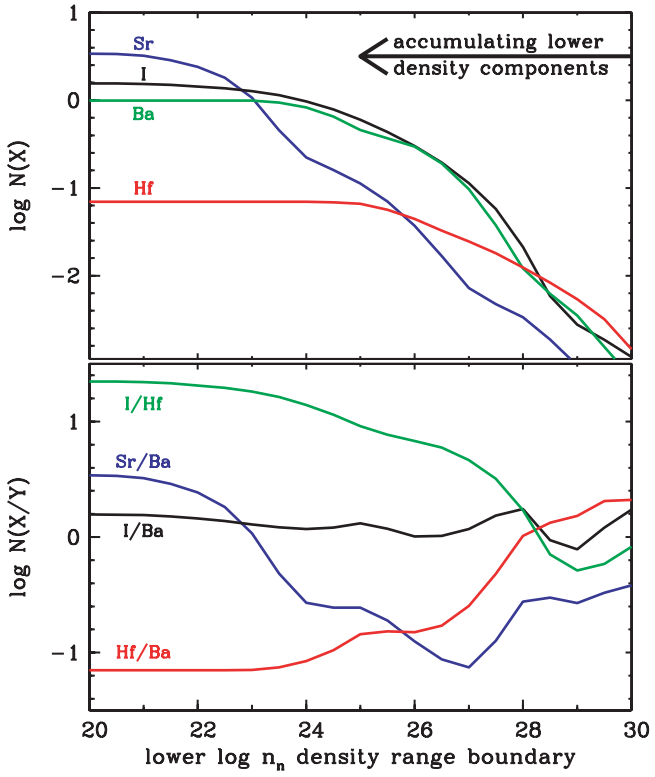

FIG. 11.—Abundance variations of Sr, I, Ba, and Hf as a function of neutron number density range; N is the abundance on the standard meteoritic scale, where $\log N_{\rm Si} = 6$. *Top*: Weighted abundance accumulations of each element. These are computed starting with the predicted abundances at the highest neutron density, $\log n_n = 30$, and adding the abundances at successively lower values of $\log n_n$. The abundances of particular elements "saturate" at their SS r-process numbers, when the contributions of even smaller neutron density regimes cease to add to their abundances. *Bottom*: Variations of selected ratios of the abundances.

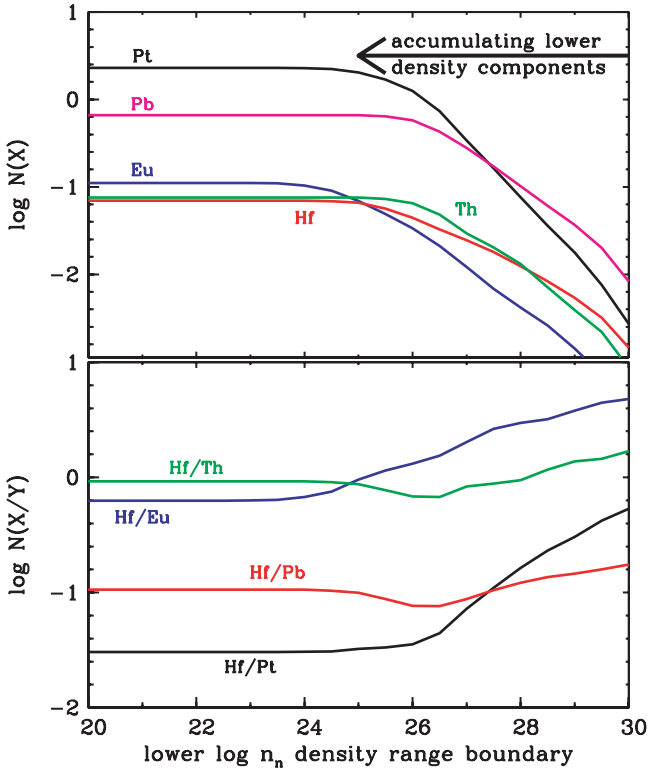

FIG. 12.—Abundance variations of Eu, Hf, Pt, Pb, and Th as functions of neutron number density range. The meanings of the curves are as in Fig. 11.

What is more important in Figure 11 is the close tracking between I and Ba in our computations. These neighboring elements correlate over a wide neutron density range; the slope of their abundance ratio shown in the bottom panel of Figure 11 is essentially flat. The situation for I and "distant" Hf ($\Delta Z = 19$) is somewhat different. Here, large differences (factors of 2 or more) occur for "high" neutron densities, $\log n_n \gtrsim 25$. These also are conditions where the Ba abundance is no longer solar. For conditions of a main r-process with full solar I, Ba, and Hf r-abundances (i.e., $23 < \log n_n < 28$), iodine at the top of the $A = 130 N_{r,\odot}$ peak and hafnium at the onset of the $A = 195 N_{r,\odot}$ peak are "coupled" ($[{\rm I/Hf}]_{r,\odot} \simeq 0.85$). Thus, for the conditions in the main r-process I, Ba, and Hf appear to be synthesized together, and in solar proportions. Sizable abundance "decouplings" of these three elements only occur at the highest neutron densities, $\log n_n \gtrsim 25$, when [I/Hf] and [Hf/Ba] do not retain their solar r-process abundance ratios.

For main r-process conditions, $23 < \log n_n < 28$, we estimate that both the abundance level of iodine and the (I/Hf) ratio are approximately 90% of their SS r-process values. In the context of our r-process model, this conclusion seems quite robust and results from two primary factors. First, from nuclear-structure arguments there is a bottleneck behavior in the r-process flow at the $N = 82$ shell closure. Thus, full-solar r-process Ba production is accompanied by the full-solar $A = 130$ abundance peak synthesis; at least at its top. Second, the "classical" r-process reaches (or enters) the $N = 82$ shell at *lower* Z than the top of the peak (^{129}Ag or ^{130}Cd). Our parameterized r-process waiting-point predictions, as well as the preliminary Farouqi et al. (2006) dynamic calculations, show that $N = 82$ is already reached in the Tc ($Z = 43$) isotopic chain, in the very extreme even in the Zr ($Z = 40$) chain. Hence, the "dividing line" between the two r-processes appears to fall well below the ^{129}Ag, because of the $N = 82$ shell closure far from stability. Instead, ^{129}Ag is included with the "rising wing" of the $A = 130$ r-process–abundance peak from about $A = 125$ upwards.

3.4. *Hafnium and the Third r-Process Peak*

Hafnium ($Z = 72$) is the next element beyond the rare-earth group, and it may serve as an important link between those elements and the third r-process peak. For practical abundance determinations, we note that Hf, like all of the rare earths and the radioactive elements Th and U, is detectable in metal-poor stars via absorption lines arising from low-excitation states of the first ion (see Lawler et al. 2007). Therefore, observed ratios of Hf/Ba, Hf/Eu, Hf/Th, etc., are very insensitive to uncertainties in stellar atmospheric parameters $T_{\rm eff}$ and $\log g$. This is a happier situation than that existing for ratios involving third r-process–peak elements, such as Eu/(Os, Ir, Pt) or Th/(Os, Ir, Pt), because the third-peak elements are detectable only via their neutral species. Atmospheric parameter errors are echoed directly into such ratios. In addition, the dominant transitions of third-peak neutral species lie in the UV ($\lambda < 4000$ Å), making detections and reliable abundance determinations for these elements difficult.

In Figure 12 we show abundance variations of Eu, Hf, Pt, Pb, and Th as a function of neutron density range, in the same fashion as was done for lighter elements in Figure 11. Variations in abundance ratios of these elements (shown in Fig. 12, *bottom*) are small for neutron densities $\log n_n < 27$. Note in particular the near constancy of the Hf/Th ratio over the entire neutron density

TABLE 2
r-PROCESS PRODUCTION RATIOS

Ratio[a] (1)	Cowan et al. (1999) (2)	Fe-Seed fit1[b] (3)	Fe-Seed fit2[c] (4)	Zr-Seed (5)	Th(fit2)/X(sol) (6)
$Th/^{238}U$	1.805	1.557	1.568	1.475	...
$^{235}U/^{238}U$	1.602	1.464	1.464	1.758	...
Th/Os	0.099	0.098	0.093	0.0735	0.0750
Th/Ir	0.092	0.095	0.089	0.0676	0.0703
Th/Pt	0.024	0.026	0.024	0.0316	0.0360
Th/third peak	0.016	0.017	0.016	0.0166	0.0181
Th/Eu	0.481	0.530	0.453	0.479	0.422
Th/Hf[d]	0.897	0.864	0.862	0.637	0.462[e]

[a] Based on ETFSI-Q mass model.
[b] Based on the least-squares fit to the SS data from $A > 83$, see text.
[c] Based on the least-squares fit to the SS data from $A > 125$, see text.
[d] Based on the average of six different neutron number density ranges between 10^{20} and 10^{30}.
[e] Based on the solar *r*-process value for Hf from Lawler et al. (2007).

range of the *r*-process. Our calculations suggest that spectroscopists should invest effort in the determination of Hf abundances (using such Hf II transitions as those at 4093.15 and 3918.09 Å) to see if the ratios of Hf/Eu and Hf/Th are constant in *r*-process–rich metal-poor stars. If so, this may strengthen the use of Th/Hf in cosmochronometry studies.

4. NUCLEAR CHRONOMETERS

In this paper we have emphasized the robustness of the *r*-process production of heavy nuclei in the mass range from $A \simeq 130$ through the actinide region, as reflected in the observed abundance patterns for metal-deficient *r*-process–enriched field halo stars. Our ability to identify this pure *r*-process pattern is a consequence of the fact that one can identify low-metallicity stars for which no significant *s*-process contamination from longer lived asymptotic giant branch stars (Busso et al. 1999) has yet occurred. An important further measure of this robustness is provided by the general consistency of the stellar ages obtained with chronometers. We examine specifically both the case of the classical thorium/uranium actinide chronometer and that of the thorium/europium chronometer.

We consider again the abundance distributions of five "pure" *r*-process stars shown in Figure 1, concentrating now on the actinide chronometers ^{232}Th (hereafter simply called Th), ^{235}U, and ^{238}U (which can be formed *only* in the *r*-process). We have computed *r*-process abundances using various global mass models, constraining all of them to reproduce the SS stable *r*-process pattern, with special emphasis on fitting the *r*-process yields of the third peak and extrapolating to masses $A \simeq 250$. In Table 2 we summarize these computations. Column (2) lists abundance ratios derived from calculations described in Cowan et al. (1999). Columns (3) and (4) are these ratios from new *r*-process calculations using Fe seeds that yield the best overall fit to the stable abundance data for masses $A > 83$ ("fit1," considering all *n*-capture isotopes) and for masses $A > 125$ ("fit2," restricted to only those isotopes matched by the main *r*-process). Column (5) employs similar calculations using a Zr seed that best match the $A > 125$ nuclei. Finally, column (6) lists the Th abundance from the fit2 calculation to the present-day observed SS elemental abundances.

Table 2's Th/U production ratios lie in the range $1.475 \leq Th/^{238}U \leq 1.805$. The present computations suggest $Th/^{238}U \simeq 1.5$ for this important chronometer pair. The new lower values result from improved nuclear data. Specifically, there is a significant change in the *r*-process matter flow through the $A \simeq 130$ bottleneck region of the $N_{r,\odot}$ peak, which continues to affect the build-up of the third *r*-peak and the formation of the heaviest *r*-elements. Therefore slightly less material is shifted beyond Bi than in our earlier approach (Pfeiffer et al. 1997; Cowan et al. 1999), yielding somewhat lower $Th/^{238}U$, $^{235}U/^{238}U$, and Th/third-peak abundance ratios.

We have taken into account in a crude manner the main fission modes, spontaneous and neutron-induced, in the calculations. We make the simplifying assumption that everything beyond mass number 256 (i.e., ^{256}Cf) fissions completely, analogous to what we have done previously (e.g., Cowan et al. 1999). Furthermore, we have verified again that the known nuclei undergoing spontaneous fission for $A < 256$ make no significant contribution to the mass range $232 < A < 255$. For cases below the $A = 256$ region, new multidimensional fission barrier calculations (Möller et al. 2001; P. Möller et al. 2006, private communication) show that spontaneous and neutron-induced fission have no effect, since the barrier heights of isotopes in the *r*-process path (with $S_n < 2$ MeV) are >8 MeV. In addition, in the β-decay back to the valley of the mass parabola, the isobars still have fission barriers of 6–7 MeV. Hence, at least from the above model predictions, spontaneous and neutron-induced fission should be negligible. Our (site-independent) waiting-point approximation calculations, as well as dynamical network calculations (Farouqi et al. 2006 for the SN II high-entropy wind scenario) indicate that the amount of matter actually involved in fission in the *r*-process beyond mass number 256 is of the order of 1%–5% of the total amount of matter. The only minor effect in this mass region instead comes from β-delayed fission.

However, most all of these calculations up to now neglect possible effects from β-delayed fission (βDF), since they are generally believed to be unimportant. Nevertheless, we have tried to estimate the βDF-rates of 20 potential βDF-candidates between ^{252}Fr and ^{277}Am using the above QRPA (Quasiparticle Random Phase Approximation) model for GT and GT+FF strength functions and the recent fission barriers of Mamdouh et al. (1998; based on the ETFSI-1 mass model) by following the simple approach outlined by Kodama & Takahashi (1975). We then have compared these results with the "complete-damping" and "WKB barrier penetration" calculations of βDF-rates by Meyer et al. (1989), who used the same QRPA model for GT strength functions and the

(systematically lower) fission barriers of Howard & Möller (1980). This comparison convinces us that the effect of the βDF-mode on the final Th and U abundances is small but may not be completely negligible. It may reduce the final Th abundance by about 8% and the final U abundance by approximately 3%. This would reduce our fit2 Th/U abundance ratio from 1.568 (see Table 2) to 1.479, which would still lie within the range of acceptable ratios.

On the other hand, one might think of including the potential βDF effects in the uncertainties of the *r*-chronometer ages. For example, this would add a further uncertainty of 0.55 Gyr to the Th/Eu age of a star like CS 22892−052, or to the Th/U age of stars like CS 31082−001 or BD +17 3248.

4.1. *The* Th/U *Chronometer*

We first examine the case for the Th/U chronometer.[9] This chronometer ratio is considered ideal as the elements are *r*-process only and near each other in nuclear mass number. As we have noted, however, the one optically available uranium line is very weak in stellar spectra and blended with molecular lines, making its detection very difficult. Furthermore, for the Th/U ages to be meaningful they need to be determined in the context of (or constrained by) the abundances of other stable elements, particularly the third *r*-process−peak elements and Pb and Bi. We consider the conditions we have explored for which we obtain the best overall agreement with the observed patterns in halo stars. The mass model chosen for this purpose is the ETFSI-Q, yielding the ratios shown in Table 2.

There are only three halo stars for which there exist observational determinations of both the thorium and the uranium abundances, along with detailed abundances of many stable elements. The observed Th/U ratio for CS 31082−001 (Hill et al. 2002) is $\mathrm{Th/U} = 8.7$ [$\log(\mathrm{Th/U}) = 0.94 \pm 0.11$], while that for BD +17 3248 is $\mathrm{Th/U} = 7.6$ [$\log(\mathrm{Th/U}) = 0.88 \pm 0.10$]. For these abundance ratios and our production ratio $(\mathrm{Th/U})_0 = 1.557$, the ages for the two halo stars CS 31082−001 and BD +17 3248 are, respectively, 16.2 and 14.9 Gyr, both having uncertainties of approximately ±3−3.5 Gyr arising from observational uncertainties. Very recently a new uranium detection has been made in HE 1523−0901 by Frebel et al. (2007), who find $\mathrm{Th/U} = 7.24$ [$\log(\mathrm{Th/U}) = 0.86 \pm 0.15$] for this star.

4.2. *The* Th/Eu *Chronometer*

An alternative to the Th/U chronometer is the ratio of the abundance of the long-lived radioactive Th nucleus to the abundance of the stable *r*-process product europium. Eu is formed almost entirely in the *r*-process (e.g., Simmerer et al. 2004 and references therein) and is readily observable from the ground. The Th/U chronometer pair may be more robust and intrinsically more accurate, but determinations of both the Th and Eu abundances are available for many more halo stars than Th and U. It is important, therefore, to quantify the use of this Th/Eu chronometer and the reliability of age determinations resulting from it.

The production ratio $(\mathrm{Th/Eu})_0$ from our current study is 0.530 (Table 2). This value is slightly higher than previous values used in our age calculations (e.g., Cowan et al. 1999) and results from better nuclear data and better fits to the stellar and solar abundance data (see discussion above). The observed Th/Eu ratio for BD +17 3248 is 0.309 (Cowan et al. 2002), leading to an implied age of 10.9 Gyr. Previously determined Th/Eu ages for other *r*-process−rich halo stars (Truran et al. 2002; Cowan & Sneden 2006; Ivans et al. 2006) have in general been consistent and found to lie in the range ≃10−15 Gyr. However, the observed abundance ratio for the star CS 31082−001 (Hill et al. 2002) is significantly higher, $\mathrm{Th/Eu} = 0.603$ [$\log\epsilon(\mathrm{Th/Eu}) = -0.22 \pm 0.07$], which for our production ratio yields a very low age. This results from high U and Th abundances in this star relative to the abundances of elements in the range from Ba to the third *r*-process abundance peak, as determined by Hill et al. However, the lead abundance, resulting from the decay of Th and U, can provide a strong constraint on the abundance values and insight into the synthesis mechanisms of these radioactive actinides.

[9] For this purpose we approximate the uranium abundance as that of ^{238}U, given the significantly shorter half-life of ^{235}U ($\tau_{1/2} = 7.038 \times 10^8$ yr) compared to ^{238}U ($\tau_{1/2} = 4.468 \times 10^9$ yr). The thorium (^{232}Th) half-life is $\tau_{1/2} = 1.405 \times 10^{10}$ yr.

4.3. *The Actinide/Lead Abundance Ratio in Halo Stars*

Can the apparent single-valued *r*-process abundance pattern in the elements Ba−Pt be expected to extend beyond the Pt−Pb peak? A further constraint on the robustness of the *r*-process in the regime from the third *r*-process peak through the actinides can be provided by observations of the Th, U, and Pb abundances in metal-poor stars.

The actinide chronometers Th, ^{235}U, and ^{238}U decay directly into the lead isotopes ^{208}Pb, ^{207}Pb, and ^{206}Pb, respectively. The lead abundances, therefore, provide a measure of the abundance levels of the chronometer nuclei. Consider the following quantitative measures. The Th/Pb ratio at the time of SS formation (Lodders 2003) is $(\mathrm{Th/Pb}) = 0.04399/1.4724 = 0.02988$. The Th/Pb ratio in our *r*-process calculations is significantly higher, $(\mathrm{Th/Pb})_{r\text{-pro}} = 0.095$. This implies first that the *r*-process is responsible for of order 30% (≈0.03/0.095) of the SS abundances of the heavy lead isotopes ^{206}Pb, ^{207}Pb, and ^{208}Pb. The Th and U chronometer abundances in extremely metal-poor *r*-process−rich halo stars, therefore, also provide a measure of the expected level of Pb in these same stars. These lead levels, since they are the products of the decays of nuclei Th, ^{235}U, and ^{238}U, can in turn be used to constrain the ages of these stars as well. In this context, the high levels of Th and U cited for the halo star CS 31082−001 are inconsistent with the abundances of the platinum peak isotopes and the limits on the lead abundance for this star (Plez et al. 2004). In contrast, the adoption of the upper limit on the Pb abundance for the star BD +17 3248 (Cowan et al. 2002) yields $\log\epsilon(\mathrm{Th/Pb}) > -1.48$, and thus $\mathrm{Th/Pb} > 0.033$; this value seems consistent with the abundances of the third *r*-process−peak elements and the expected *r*-process production ratio. Also consistent are the Th/Pb ratios of 0.024 to 0.042 (depending on adopting one of the very uncertain lead values) that have been reported for CS 22892−052 (Sneden et al. 2003). More work needs to be done to understand specifically how CS 31082−001 can have such an overabundance of the actinide chronometers Th and U with a correspondingly low Pb abundance. More generally it needs to be determined if there are other such stars.

Abundances of lead in the metal-poor halo stars, while difficult to derive and ideally requiring space-based observations, offer the promise of more refined (and constraining) chronometric age determinations.

5. CONCLUSIONS

The rapid *n*-capture process is understood to be responsible for the synthesis of approximately half of all of the isotopes present in solar system matter in the mass region from approximately zinc through the actinides. While the general features of this process were identified in the classic papers by Burbidge et al. (1957) and Cameron (1957), our current understanding of the *r*-process remains incomplete. We have yet to cleanly identify which of the proposed astrophysical sites contribute significantly to the

observed abundance pattern, and we have yet to reconcile the apparent duplicity of *r*-process sites with extant models for the operation of the *r*-process in diverse astronomical environments. In this paper we have explored implications from parameterized waiting-point synthesis calculations.

Various observations suggest that contributions from two different *r*-process astronomical sites or environments are required, for the mass regimes $A \lesssim 130$ and $A \gtrsim 130$ respectively. Here, we have tried to identify the mass number that represents the dividing line between these two ("weak" and "main") *r*-process contributions. In this context, our discussions in this paper and associated calculations lead to the following conclusions.

1. The combined elemental and isotopic data on low-metallicity *r*-process–rich stars confirms a robust *r*-process pattern extending over the ($A > 130$–140) *n*-capture isotopic domain.

2. We are able to reproduce the total SS *r*-process abundances with a superposition of neutron number densities ranging from $\log n_n = 20$–28. Our calculations indicate that smaller neutron number densities ($\log n_n = 20$–22) that characterize the weak *r*-process are required to reproduce the $A = 80$–100 SS isotopic *r*-process abundances. We estimate that the division between weak and main *r*-process density regimes occurs at $\log n_n \simeq 23.0 \pm 0.5$. More sophisticated network calculations (Farouqi et al. 2006) appear to bear out our general results.

3. The *r*-process calculations that successfully generate the element pattern extending down to $A = 135$ indicate that the production of ^{129}I is at a level ~90% of its solar *r*-process value, relative to the Ba–Pb region. Our calculations suggest that the $^{129}\mathrm{I}/^{182}\mathrm{Hf}$ production ratio is quite compatible with the anticipated *r*-process abundance pattern. In this context, our results imply that the dividing line (in mass number) between the weak and main *r*-process components must necessarily fall below ^{129}I. We note, however, that observational limitations, so far, prevent, an exact identification of the elemental atomic number where the break occurs between the main and weak *r*-process. (Iodine, for example, has not yet been observed in a metal-poor halo star.)

4. We find that the isotopic fractions of barium and the elemental Ba/Eu abundance ratios in *r*-process–rich low-metallicity stars can only be matched by computations in which the neutron densities are in the range $23 \lesssim \log n_n \lesssim 28$, values typical of the main *r*-process. For the main *r*-process our calculations predict a solar *r*-process value of the Ba isotopic ratio, $f_{\mathrm{odd}} \equiv [N(^{135}\mathrm{Ba}) + N(^{137}\mathrm{Ba})]/N(\mathrm{Ba}) \simeq 0.47$–$0.50$. The observed value of $f_{\mathrm{odd}} = 0.3 \pm 0.21$ in one metal-poor halo star is consistent with the SS *r*-process ratio. While the uncertainty is large and does not rule out some slight *s*-process production, the elemental ratio of [Ba/Eu] in this star is in agreement with the SS *r*-process only ratio. Since this star's Ba/Eu elemental abundance ratio is also confirmed by our calculations, an *r*-process–only origin for its Ba isotopes is strongly indicated.

5. In the neutron number density ranges required for production of the observed solar/stellar third *r*-process peak ($A \approx 200$), the predicted abundances of interpeak element hafnium ($Z = 72$, $A \approx 180$) follow closely those of third-peak elements (osmium through platinum) and lead. This suggests that abundance comparisons of hafnium to both rare-earth and third-peak elements can shed further light on claims of invariance in the entire heavy end of the *r*-process abundance pattern. Hafnium, observable from the ground and close in mass number to the third *r*-process–peak elements, could be used as a new nuclear chronometer pair Th/Hf for age determinations, particularly for cases in which U is not detected. In the context of the calculations that reproduce the stable SS *r*-process abundances, we have determined several important chronometric production ratios including Th/U, Th/Eu, Th/Pt, and Th/third-peak elements and Th/Hf. For example, the present computations suggest $\mathrm{Th}/^{238}\mathrm{U} \simeq 1.5$ for this chronometer pair. These newly predicted chronometric ratios can then be employed to determine ages in stars where Th or U have been detected.

We thank Roberto Gallino, Peter Möller, Anna Frebel, and Uli Ott for useful discussions and an anonymous referee for helpful suggestions. This work has been supported in part by the Deutsche Forschungsgemeinschaft (DFG) under contract KR 806/13-1, and the Helmholtz Gemeinschaft under grant VH-VI-061 and by GSI (Univ. Mainz F+E-Vertrag [MZ/KLK]). Support was also provided by the National Science Foundation under grants AST 03-07279 (J. J. C.), AST 03-07495 (C. S.), and the Physics Frontier Center (JINA) PHY 02-16783 (J. W. T.), by the DOE under contract B523820 to the ASCI Alliances Center for Astrophysical Flashes (J. W.T.), and at the Argonne National Laboratory, which is operated under contract W-31-109-ENG-38 (J. W. T.).

REFERENCES

Aboussir, Y., Pearson, J. M., Dutta, A. K., & Tondeur, F. 1995, At. Data Nucl. Data Tables, 61, 127
Anders, E., & Grevesse, N. 1989, Geochim. Cosmochim. Acta, 53, 197
Aoki, W., Honda, S., Beers, T. C., & Sneden, C. 2003a, ApJ, 586, 506
Aoki, W., et al. 2003b, ApJ, 592, L67
———. 2005, ApJ, 632, 611
Arlandini, C., Käppeler, F., Wisshak, K., Gallino, R., Lugaro, M., Busso, M., & Straniero, O. 1999, ApJ, 525, 886
Audi, G., Bersillon, O., Blachot, J., & Wapstra, A. H. 2003, Nuc. Phys. A, 729, 3
Barklem, P. S., et al. 2005, A&A, 439, 129
Burbidge, E. M., Burbidge, R. R., Fowler, W. A., & Hoyle, F. 1957, Rev. Mod. Physics, 29, 547
Burris, D. L., Pilachowski, C. A., Armandroff, T. A., Sneden, C., Cowan, J. J., & Roe, H. 2000, ApJ, 544, 302
Busso, M., Gallino, R., & Wasserburg, G. J. 1999, ARA&A, 37, 239
Cameron, A. G. W. 1957, Chalk River Report CRL-41
Christlieb, N., et al. 2004, A&A, 428, 1027
Cowan, J. J., Pfeiffer, B., Kratz, K.-L., Thielemann, F.-K., Sneden, C., Burles, S., Tytler, D., & Beers, T. C. 1999, ApJ, 521, 194
Cowan, J. J., & Sneden, C. 2006, Nature, 440, 1151
Cowan, J. J., Sneden, C., Den Hartog, E. A., & Collier, J. 2006, in Proc. NASA Laboratory Astrophysics Workshop, ed. P. F. Weck, V. H. S. Kwong, & F. Salama (Washington: NASA), 82
Cowan, J. J., & Thielemann, F.-K. 2004, Phys. Today, 57, 47
Cowan, J. J., Thielemann, F.-K., & Truran, J. W. 1991, Phys. Rep., 208, 267
Cowan, J. J., et al. 2002, ApJ, 572, 861
Den Hartog, E. A., Herd, T. M., Lawler, J. E., Sneden, C., & Cowan, J. J., & Beers, T. C. 2005, ApJ, 619, 639
Den Hartog, E. A., Lawler, J. E., Sneden, C., & Cowan, J. J. 2003, ApJS, 148, 543
———. 2006, ApJS, 167, 292
Dillmann, I., et al. 2003, Phys. Rev. Lett., 91, 162503
Dobaczewski, J., Hamamoto, I., Nazarewicz, W., & Sheikh, J. A. 1996, Phys. Rev. Lett., 72, 981
Farouqi, K., Freiburghaus, C., Kratz, K.-L., Pfeiffer, B., Rauscher, T., & Thielemann, F.-K. 2005, Nuc. Phys. A, 758, 631
Farouqi, K., Kratz, K.-L., Pfeiffer, B., Rauscher, T., & Thielemann, F.-K. 2006, in AIP Conf. Proc. 819, Capture Gamma-Ray Spectroscopy and Related Topics, ed. A. Woehr (Berlin: Springer), 419
Frebel, A., Christlieb, N., Norris, J. E., Thom, C., Beers, T. C., & Rhee, J. 2007, ApJ, 660, L117
Freiburghaus, C., Rembges, J.-F., Rauscher, T., Thielemann, F.-K., Kratz, K.-L., Pfeiffer, B., & Cowan, J. J. 1999a, ApJ, 516, 381
Freiburghaus, C., Rosswog, S., & Thielemann, F.-K. 1999b, ApJ, 525, L121
Goriely, S., Samyn, M., Pearson, J. M., & Onsi, M. 2005, Nuc. Phys. A, 750, 425

Goriely, S., Tondeur, F., & Pearson, J. M. 2001, At. Data Nucl. Data Tables, 77, 311
Gratton, R., & Sneden, C. 1994, A&A, 287, 927
Hauge, Ø. 1972, Sol. Phys., 27, 286
Hilf, E. R., et al. 1976, CERN-Rep. 76-13, 142
Hill, V., et al. 2002, A&A, 387, 560
Honda, S., Aoki, W., Kajino, T., Ando, H., Beers, T. C., Izumiura, H., Sadakane, K., & Takada-Hidai, M. 2004, ApJ, 607, 474
Howard, W. M., & Möller, P. 1980, At. Data Nucl. Data Tables, 25, 219
Ivans, I. I., Simmerer, J., Sneden, C., Lawler, J. E., Cowan, J. J., Gallino, R., & Bisterzo, S. 2006, ApJ, 645, 613
Johnson, J. A. 2002, ApJS, 139, 219
Johnson, J. A., & Bolte, M. 2001, ApJ, 554, 888
Käppeler, F., Beer, H., & Wisshak, K. 1989, Rep. Prog. Phys., 52, 945
Kodama, T., & Takahashi, K. 1975, Nucl. Phys. A, 239, 489
———. 2006, in AIP Conf. Proc. 819, Capture Gamma-Ray Spectroscopy and Related Topics, ed. A. Woehr (Berlin: Springer), 409
Kratz, K.-L., Bitouzet, J.-P., Thielemann, F.-K., Möller, P., & Pfeiffer, B. 1993, ApJ, 403, 216
Kratz, K.-L., Ostrowski, A. N., & Pfeiffer, B. 2005a, in AIP Conf. Proc. 769, International Conference on Nuclear Data for Science and Technology, ed. R. C. Haight (Melville: AIP), 1356
Kratz, K.-L., Pfeiffer, B., & Thielemann, F.-K. 1998, Nuc. Phys. A, 630, 352
Kratz, K.-L., Pfeiffer, B., Thielemann, F.-K., & Walters, W. B. 2000, Hyperfine Interactions, 129, 185
Kratz, K.-L., Thielemann, F.-K., Hillebrandt, W., Möller, P., Harms, V., & Truran, J. W. 1988, J. Phys. G, 14, 331
Kratz, K.-L., et al. 2005b, European J. Phys. A Suppl., 25, 633
Lambert, D. L., & Allende Prieto, C. 2002, MNRAS, 335, 325
Lattimer, J. M., Mackie, F., Ravenhall, D. G., & Schramm, D. N. 1977, ApJ, 213, 225
Lawler, J. E., Den Hartog, E. A., Labby, Z. E., Sneden, C., Cowan, J. J., & Ivans, I. I. 2007, ApJS, 169, 120
Lawler, J. E., Den Hartog, E. A., Sneden, C., & Cowan, J. J. 2006, ApJS, 162, 227
Lawler, J. E., Wickliffe, M. E., Den Hartog, E. A., & Sneden, C. 2001, ApJ, 563, 1075
Lodders, K. 2003, ApJ, 591, 1220
Lunney, D., Pearson, J. M., & Thibault, C. 2003, Rev. Mod. Phys. 75, 1021
Magain, P. 1995, A&A, 297, 686
Mamdouh, A., Pearson, J. M., Rayet, M., & Tondeur, F. 1998, Nucl. Phys. A, 644, 389
Meyer, B. S., & Clayton, D. D. 2000, Sp. Sci. Rev., 92, 133
Meyer, B. S., Howard, W. M., Mathews, G. J., Takahashi, K., Möller, P., & Leander, G. A. 1989, Phys. Rev. C, 39, 1876
Möller, P., Madland, D. G., Sierk, A. J., & Iwamoto, A. 2001, Nature, 409, 785
Möller, P., Nix, J. R., & Kratz, K.-L. 1997, At. Data Nucl. Data Tables, 66, 131
Möller, P., Nix, J. R., Myers, W. D., & Swiatecki, W. J. 1995, At. Data Nucl. Data Tables, 59, 185
Möller, P., Pfeiffer, B., & Kratz, K.-L. 2003, Phys. Rev. C, 67, 055802
Möller, P., & Randrup, J. 1990, Nucl. Phys. A, 514, 1
O'Brien, S., Dababneh, S., Heil, M., Käppeler, F., Plag, R., Reifarth, R., Gallino, R., & Pignatari, M. 2003, Phys. Rev. C, 68, 035801
Pearson, J. M. 2004, in The *r*-Process: The Astrophysical Origin of the Heavy Elements and Related Rare Isotope Accelerator Physics, ed. Y.-Z. Qian (Singapore: World Scientific), 43
Pearson, J. M., Nayak, R. C., & Goriely, S. 1996, Phys. Lett. B, 387, 455
Pfeiffer, B., Kratz, K.-L., & Möller, P. 2002, Prog. Nuc. Energy, 41, 39
Pfeiffer, B., Kratz, K.-L., & Thielemann, F.-K. 1997, Z. Phys. A, 357, 23
Pfeiffer, B., Kratz, K.-L., Thielemann, F.-K., & Walters, W. B. 2001, Nucl. Phys. A, 693, 282
Plez, B., et al. 2004, A&A, 428, L9
Qian, Y. Z., & Wasserburg, G. J. 2000, Phys. Rep., 333, 77
Rauscher, T. 2004, in The *r*-Process: The Astrophysical Origin of the Heavy Elements and Related Rare Isotope Accelerator Physics, ed. Y.-Z. Qian (Singapore: World Scientific), 63
Rauscher, T., & Thielemann, F.-K. 2000, At. Data Nucl. Data Tables, 75, 1
Rikovska-Stone, J. 2005, J. Phys. G, 31, R211
Rosswog, S., Liebendorfer, M., Thielemann, F.-K., Davies, M. B., Benz, W., & Piran, T. 1999, A&A, 341, 499
Samyn, M., Goriely, S., Bender, M., & Pearson, J. M. 2004, Phys. Rev. C, 70, 044309
Simmerer, J., Sneden, C., Cowan, J. J., Collier, J., Woolf, V., & Lawler, J. E. 2004, ApJ, 617, 1091
Sneden, C., & Cowan, J. J. 2003, Science, 299, 70
Sneden, C., Cowan, J. J., Lawler, J. E., Burles, S., Beers, T. C., & Fuller, G. M. 2002, ApJ, 566, L25
———. 2003, ApJ, 591, 936
Spite, M., & Spite, F. 1978, A&A, 67, 23
Takahashi, K., Witti, J., & Janka, H.-T. 1994, A&A, 286, 857
Thielemann, F.-K., Kratz, K.-L., Pfeiffer, B., Rauscher, T., van Wormer, L., & Wiescher, M. 1994, Nucl. Phys. A, 570, 329
Travaglio, C., Gallino, R., Arnone, E., Cowan, J., Jordan, F., & Sneden, C. 2004, ApJ, 601, 864
Truran, J. W., Cowan, J. J., Pilachowski, C. A., & Sneden, C. 2002, PASP, 114, 1293
Wanajo, S., Goriely, S., Samyn, M., & Itoh, N. 2004, ApJ, 606, 1057
Wasserburg, G. J., Busso, M., & Gallino, R. 1996, ApJ, 466, L109
Westin, J., Sneden, C., Gustafsson, B., & Cowan, J. J. 2000, ApJ, 530, 783
Wisshak, K., Voss, F., Käppeler, F., Kazakov, L., & Reffo, G. 1998, Phys. Rev. C, 57, 391
Woosley, S. E., Wilson, J. R., Mathews, G. J., Hoffman, R. D., & Meyer, B. S. 1994, ApJ, 433, 229